MULTIFRACTAL ANALYSIS OF RESTING STATE NETWORKS IN FUNCTIONAL MRI

Philippe Ciuciu, Gaël Varoquaux, Patrice Abry, Moty Almog

MULTIFRACTAL ANALYSIS OF RESTING STATE NETWORKS IN FUNCTIONAL MRI

Philippe Ciuciu[(1)*], *Gaël Varoquaux*[(2)], *Patrice Abry*[(3)] *and Moty Almog*[(1)]

[(1)]LNAO/NeuroSpin, CEA Saclay, Bat. 145, 91191 Gif-sur-Yvette, cedex France
[(2)] INSERM U992 and INRIA Saclay Parietal project, NeuroSpin, 91191 Gif-sur-Yvette, cedex France
[(3)] CNRS, UMR 5672, Laboratoire de Physique. ENS Lyon, France.
[1] firstname.lastname@cea.fr, [2] gael.varoquaux@normalesup.org, [3] patrice.abry@ens-lyon.fr

ABSTRACT

It has been know for at least one decade [1] that functional MRI time series display long-memory properties, such as power-law scaling in the frequency spectrum. Concomitantly, multivariate model-free analysis of spatial patterns , such as spatial Independent Component Analysis (sICA) [2], has been successfully used to segment from spontaneous activity Resting-State Networks (RSN) that correspond to known brain function. As recent neuroscientific studies suggest a link between spectral properties of brain activity and cognitive processes [3], a burning question emerges: can temporal scaling properties offer new markers of brain states encoded in these large scale networks? In this paper, we combine two recent methodologies: group-level canonical ICA for multi-subject segmentation of brain network, and wavelet leader-based multifractal formalism for the analysis of RSN scaling properties. We identify the brain networks that elicit self-similarity or multifractality and explore which spectral properties correspond specifically to known functionally-relevant processes in spontaneous activity.

Index Terms— spatial ICA, multifractality, scaling, resting state, fMRI

1. INTRODUCTION

The presence of scale invariance in functional MRI (fMRI) data has been considered as confound or noise for a long time. Preliminary evidence that fMRI time series have long memory in time or $1/f$ spectral properties has been demonstrated on "resting state" motion-corrected datasets [1]. Physiological factors such as cardiac beat or breathing cycle may also contribute to this scaling phenomenon since they contaminate the Blood Oxygenated Level Dependent (BOLD) signal with properties depending on the sampling period of data (i.e. short/long time of repetition (TR)) [4]. Early investigations therefore considered these space-varying low frequency components as noise, responsible for potential non stationarities.

Other authors pointed out that the BOLD signal itself contains power at virtually all frequencies, notably in randomized event-related designs [5]. Interestingly, recent studies have reported that low-frequency spatial fluctuations in cortical BOLD signals may be indicative of synchronized long memory neuronal oscillations rather than merely noise [6, 7]. Concomitantly, greater persistence during brain activation has been found in normal subjects in [6]. Also, higher predictability summarized in terms of scaling exponent (controlling the power law decrease of $1/f$ spectra) has been reported in patients with Alzheimer disease or with major depressive disorder, especially in brain regions implicated in the early stages of the degeneracy process [7, 8]. More recently, scale invariance has been demonstrated to be an intrinsic property of ongoing brain activity. It may thus provide a new insight on how the brain works provided that quantitative parameters can be mapped with good specificities to cognitive states (resting or awake states), task performance, or neurological disorder (epilepsy) [3]. These last works relied on tools such as windowed-averaged periodograms which are grounded on assumptions self-similarity. However, the empirical results in [3] (Hurst parameter larger than 1) show that the data cannot be considered as realizations of fractional Brownian motion noise, for which scaling properties are controlled by the sole self-similarity (or Hurst) parameter lying in the range $[0, 1]$. A richer description is thus needed to reflect the signal properties.

Inspired by the connection between $1/f$ and long range dependence, several groups have argued that the analysis of fMRI time series should be performed in the wavelet domain [9–11]. A first attempt to identify stimulus-induced signal changes from scaling parameters was proposed in [6, 12]. These authors developed a voxel-based fluctuation analysis (FA) and applied it to high temporal resolution fMRI data. Interestingly, they showed that fractal features of voxel time series can discriminate active from inactive brain regions [6, 12]. Also, to decide whether scaling analysis can help to distinguish motion artifacts from true BOLD responses, complementary analyses were conducted in [13]. They are based on detrended fluctuation analysis (DFA) and conclude that DFA succeeds in distinguishing amongst three types of voxels, noise, motion artifacts, and true BOLD responses when the classical FA fails to robustly recognize which active regions in the brain are truly involved in certain tasks. However, it has been argued in [14] that wavelet tools perform better than DFA. Moreover, while scale invariance was first modeled with $1/f$ processes and long range dependence, these classes of models have fruitfully been embodied into the larger description of self-similar processes. More recently, multifractal (MF) processes were proposed has another versatile class of models for scale invariance. Therefore, akin to [11, 15], in the present contribution, the analysis of scale invariance is based on the recently introduced wavelet Leaders [16], a tool which, compared to those listed above, brings in two major benefits: *i)* it shows by far the best estimation performance, and *ii)* it enables to discriminate efficiently multifractality from self-similarity or long memory.

However, in [11, 15], due to voxelwise analysis and between-voxel variability, the MF spectra suffered from a lack of robustness in certain brain regions. To overcome these drawbacks, here we make use of a multivariate approach, i.e. spatial Independent Component Analysis (sICA), which has been popularized in the last decade as an exploratory or model-free approach for analyzing fMRI

data [2, 17]. Hence, it appears as the method of choice for studying resting-state datasets. At the group-level however, classical sICA schemes (group ICA, tensor ICA,...) lack of reproducibility due to between-subject variability. Also, statistical decision rules may appear too conservative. This has motivated the development of the canonical ICA (canICA) methodology, which relies on a generalized canonical analysis to find out reproducible components across subjects [18]. In this paper, canICA is used to segment salient features from multi-subject resting-state datasets, thus decomposing the multivariate datasets in a product of K spatial components and associated time series. The wavelet leader based multifractal analysis is applied to these time-series, to differentiate functional processes encoded in RSNs from other brain regions in terms of scaling exponents.

The remainder of the paper is organized as follows. Section 2 summarizes the canICA framework we rely on. Then, Section 3 introduces the key notions underlying multifractal analysis as well as the wavelet Leader-based multifractal formalism that permits to analyze precisely the scaling properties in empirical data. Section 4 is devoted to experimental results and group-level statistical analysis on the multifractal parameters. Conclusion are drawn in Section 6.

2. FROM SPONTANEOUS-ACTIVITY RECORDINGS TO BRAIN-NETWORK TIME SERIES

In this section, we describe how the time-series used to perform multifractal analysis are extracted from multi-subject fMRI resting-state datasets. Let us denote $\left\{\boldsymbol{Y}^s \in \mathbb{R}^{T \times P}, s = 1 : S\right\}$ S datasets composed of T images with P voxels. We apply an ICA-based analysis [19] to decompose the original voxelwise signals into K subject-specific time series $\boldsymbol{X}^s \in \mathbb{R}^{T \times K}$ and group-level spatial components $\boldsymbol{A} \in \mathbb{R}^{K \times P}$, with residuals $\boldsymbol{N}^s$:

$$\forall s = 1 : S, \quad \boldsymbol{Y}^s = \boldsymbol{X}^s \boldsymbol{A} + \boldsymbol{N}^s. \tag{1}$$

The spatial maps $\boldsymbol{A}$ segment salient and reproducible features of resting-state fluctuations such as brain functional networks or structured noise (eg physiological or movement artifacts). Note however that no ICA ever guarantees any independence (or gives a p-value). The corresponding subject-specific time series $\boldsymbol{X}^s$ will be used in subsequent scaling analysis. In the following, we summarize how $\boldsymbol{A}$ is derived.

2.1. Generative model for the spatial patterns

The spatial features of interest $\boldsymbol{A}$ are observed mixed together and confounded by unstructured background noise, inter-subject variability, and observation noise. More specifically, following [18, 19], the observed signal can be written as a generative model made of hierarchical decompositions with different noise terms at each level. First, we model group-level patterns, $\boldsymbol{C} \in \mathbb{R}^{K \times N}$, as generated by the set of sources $\boldsymbol{A} \in \mathbb{R}^{K \times N}$, confounded by additive unstructured noise $\boldsymbol{E} \in \mathbb{R}^{K \times N}$, and observed as a random linear mixture in the group-level signal sub-space spanned by $\boldsymbol{C}$:

$$\boldsymbol{C} = \boldsymbol{M}\boldsymbol{A} + \boldsymbol{E},$$

where $\boldsymbol{M}$ is an orthogonal mixing matrix. Each subject s is described by patterns $\boldsymbol{P}^s$, generated from linear combinations of the group-level patterns $\boldsymbol{C}$ and additional within-subject variability $\boldsymbol{R}^s$:

$$\forall s = 1 : S, \quad \boldsymbol{P}^s = \boldsymbol{\Lambda}^s \boldsymbol{C} + \boldsymbol{R}^s,$$

where $\boldsymbol{\Lambda}^s$ is a subject-specific loading matrix. Finally, each image in the observed data is a combination of different subject-specific patterns $\boldsymbol{P}^s$ confounded by observation noise:

$$\forall s = 1 : S \quad \boldsymbol{Y}^s = \boldsymbol{W}^s \boldsymbol{P}^s + \boldsymbol{T}^s.$$

To summarize, Eq. (1) holds provided that $\boldsymbol{X}^s = \boldsymbol{W}^s \boldsymbol{\Lambda}^s \boldsymbol{M}$ and $\boldsymbol{N}^s = \boldsymbol{W}^s \boldsymbol{\Lambda}^s \boldsymbol{E} + \boldsymbol{W}^s \boldsymbol{R}^s + \boldsymbol{T}^s$.

2.2. CanICA estimation procedure

Starting from the available datasets $\{\boldsymbol{Y}^s, s = 1 : S\}$, we first select $\boldsymbol{P}^s$ using Principal Component Analysis (PCA) to maximize subject-level explained variance. Second, group-level components $\boldsymbol{C}$ are computed using generalized canonical correlation to select only components reproducible across subjects [19]. Finally, sparse and non-overlapping spatial sources $\boldsymbol{A}$ are extracted using ICA on $\boldsymbol{C}$ followed by thresholding to control for unstructured noise $\boldsymbol{E}$ [18]. The number of components K and the threshold are set with a p-value of $5 \cdot 10^{-2}$ according to [18, 19].

Note that spatial ICA procedures favor high kurtosis, and thus components that are either super-Gaussian or sub-Gaussian. Super Gaussian components can be seen as sparse components confounded with Gaussian noise. In this regards, CanICA is not special, and the importance of sparsity in ICA analysis of fMRI data has been outlined elsewhere [20].

3. SCALING AND MULTIFRACTAL ANALYSIS

3.1. Scale invariance (or scaling)

In numerous modern applications, real-worl data are well-described by the scale invariance (or scaling) paradigm. Conventional modeling of time series relies on the identification of a single, or a few, characteristic time scales or frequency bands, that play a central role. Conversely, in the scale invariance paradigm, the modeling stems from a mechanism that gives a relationship between all the scales in the data, that hence are all of equal importance. The intuition beyond scale invariance is often quantified through wavelet coefficients. In this section we give the mathematical formalism underlying the scaling properties we wish to investigate, but also and most-importantly, we outline state-of-the-art analysis tools to estimate the corresponding parameters on short time series, such as those encountered in fMRI.

3.2. Scaling, wavelet coefficients and multifractal analysis

In what follows, we drop the subject superscript s. Let $d_X(j, n)$ denote the (L^1-normalized) discrete wavelet transform coefficients of a componentwise subject-specific time series X (eg column $\boldsymbol{x}_c$ in $\boldsymbol{X}$ in Eq. (1)), where j refers to the analysis scale ($a = 2^j$) and n to the time position ($t = 2^j n$), computed from a *mother-wavelet* $\psi_0(t)$. Scale invariance often refers to the fact that $S_d(j, q)$, the time averages of the q-th power of the wavelet coefficients $d_X(j, n)$, behave as power-laws with respect to the analysis scales $a = 2^j$, over a large range of scales (cf. e.g., [16]):

$$S_d(j, q) \triangleq \frac{1}{N_j} \sum_{n=1}^{N_j} |d_X(j, n)|^q \simeq c_q 2^{j \zeta_d(q)}. \tag{2}$$

The function $\zeta_d(q)$, usually termed the *scaling exponents*, is then commonly used into data classification tasks. Its popularity stems from its deep relationship to the multifractal properties of the time

series X. Indeed, another important quantity often used to characterize the complexity of empirical data is the multifractal spectrum $D(h)$. It consists of the Haussdorf dimension of the set of time positions, t_k, on the real line, where the local regularity of X is well described by the same regularity (or Hölder) exponent h. Therefore, $D(h)$ measures globally and statistically how wide are the fluctuations in time of the local regularity $h(t)$ of X [21]. A Legendre transform of $\zeta_d(q)$ yields a concave upper bound of $D(h)$: $\min_{q \neq 0}(1 + qh - \zeta_d(q)) \geq D(h)$ [21]. It is here crucial to note that a correct estimation of $D(h)$ requires the use of both positive and negative values of q. For further introduction to multifractal analysis, the reader is referred to e.g. [16, 21]. It is however well-known that this upper bound is poor, especially for negative values of q. Recently, it has been shown [16] that this can be significantly improved, both theoretically and practically, by replacing the wavelet coefficients $d_X(j, n)$ by wavelet Leaders $L_X(j, n)$.

3.3. Wavelet Leaders and multifractal analysis

Let $\lambda_{j,n}$ denote the dyadic intervals, $\lambda_{j,n} = [n2^j, (n+1)2^j)$, and $3\lambda_{j,n} = \bigcup_{m\{-1,0,1\}} \lambda_{j,n+m}$. The wavelet leaders $L_X(j, n)$ are defined as $L_X(j, n) = \sup_{\lambda' \subset 3\lambda_{j,n}} |d_X(\lambda')|$ [16]. Thus, they consist of the local suprema of the wavelet coefficients located within a certain spatial neighborhood, and over all finer scales. Scale invariance can now be reformulated as:

$$S_L(j, q) \triangleq \frac{1}{N_j} \sum_{n=1}^{N_j} L_X(j, n)^q \simeq c_q 2^{j\zeta_L(q)}. \tag{3}$$

The wavelet Leader based scaling exponents, $\zeta_L(q)$, have been shown to offer, compared to the wavelet coefficient based ones [16]: *i.)* a better mathematically grounded analysis of the multifractal and scaling properties of the data; *ii.)* a much tighter bound for $D(h)$, notably by allowing the efficient use of negative qs; *iii.)* a significantly improved estimation of the scaling exponents, in terms of statistical performance. In practice, this permits to address efficiently important issues such as: *a.)* are the data short-range dependent (SRD) or long-range dependent (LRD)? *b.)* are the data monofractal (or self-similar) or truly multifractal? This latter question can be recast practically into that of testing whether $\zeta_L(q)$ (or $\zeta_d(q)$) consists of a linear or concave function of q or not [16, 21].

3.4. Log-cumulants and estimation

Measuring the scaling exponents for all q leads to a large collection of highly correlated estimates that may turn uneasy to use practically. Instead, it has been proposed to use polynomial expansions of $\zeta_L(q) = \sum_{p \geq 1} c_p^L q^p/p\,!$. It has further been shown [16] that the c_p^L can be obtained from the scale dependence of the cumulant of order $p \geq 1$, $\mathcal{C}^L(j, p)$, of the random variable $\ln L_X(j, \cdot)$:

$$\forall p \geq 1, \quad \mathcal{C}^L(j, p) = c_{0,p}^L + c_p^L \ln 2^j. \tag{4}$$

Therefore, the $\{c_p^L, p \geq 1\}$ summarize efficiently the function $\zeta_L(q)$ and hence of $D(h)$. In practice, for short time series, such as those commonly processed in the fMRI context, c_1^L and c_2^L gather most of the information actually available from data. This is of major practical interest because self-similar processes are characterized by $\forall p \geq 2 : c_p^L \equiv 0$, while for multifractal processes of interest $c_2^L \neq 0$. Also, c_1^L is closely related to Hurst parameter characterizing self-similarity and LRD [11, 16, 21]. Eqs. (3)–(4) above led to

estimate the $\zeta^L(q)$ and c_p^L by linear regressions:

$$\hat{\zeta}^L(q) = \sum_{j=j_1}^{j_2} w_j \log_2 S^L(j, q), \quad \hat{c}_p^L = \log_2 e \sum_{j=j_1}^{j_2} w_j \hat{\mathcal{C}}^L(j, p).$$

This has been thoroughly studied in [11, 16] and is not further detailed here. The same expansion can be conducted for he wavelet coefficient based $\zeta_d(q) = \sum_{p \geq 1} c_p^d q^p/p\,!$ and therefore the same estimation procedures can be used.

4. EXPERIMENTAL RESULTS

4.1. Description of the datasets

We consider the set of brain resting-state time series used in [19]. Twelve healthy volunteers were scanned twice at rest ($TR = 1.5$s.), eyes closed, for a period of 20 minutes during each session. Each individual dataset consists of of two sessions, each being made of $n = 820$ volumes (time points) with a 3 mm isotropic resolution, corresponding to approximately $50\,000$ voxels within the brain. Standard neuroimaging preprocessing was applied using the SPM5 software[1]: after motion correction, cerebral volumes were realigned to an inter-subject template and smoothed with a 6 mm isotropic Gaussian kernel. Next, as explained in Section 2, CanICA was applied to the whole dataset to exhibit the group-level spatial components (or sources) $\boldsymbol{A}$ and the subject- and source-specific time series $\boldsymbol{X}^s$. As indicated in Section 2, our tresholding procedure generated $K = 42$ components for $\boldsymbol{A}$. Finally, the multifractal spectrum $D(h)$ associated with each component-specific time series in matrix $\{\boldsymbol{X}^s, s = 1 : S\}$ was computed. To this end, we only focused on the leader-based scaling exponents $\zeta_L(q)$ for a range of statistical orders $q \in [-10, 10]$. Scale invariance was observed within a 3-octave range of scales corresponding to [12, 192] seconds. In practice, we restited the polynomial expansions of $\zeta_L(q)$ to the estimation of (c_1^L, c_2^L) from each time series. In what follows, we drop the superscript L for conciseness and derive group-level statistical tests to assess the scaling properties of the spatial components and to localize which of them exhibit multifractal behaviour or not.

4.2. Group-level Statistical analysis

The goal now consists in assessing the statistical significance at the group level of the two first multifractal coefficients $(c_{1,k}^s, c_{2,k}^s)$ computed for every spatial component k and subject s. More precisely, we perform the following *one-sided* tests, $\forall k = 1 : K$:

$$\left.\begin{array}{lll} H_0^{(1,k)} : c_{1,k} & \leqslant 0.5, & \text{(White noise or SRD)} \\ H_0^{(2,k)} : c_{2,k} & = 0., & \text{(H-sssi process)}, \end{array}\right\} \tag{5}$$

where H-sssi stands for H self-similar process with stationary increments (or monofractal). On the one hand, rejecting $H_0^{(1,k)}$ clearly amounts to localizing brain areas or components eliciting temporal long range dependencies. On the other hand, rejecting $H_0^{(2,k)}$ enables to discriminate multifractality from self-similarity.

Since there is no evidence in the data that the scaling parameters are normally distributed across subjects, we use nonparametric tests and different statistics (Student t, Wilcoxon's signed rank (WSR) statistic, Empirical Likelihood Ratio), the t-score statistics being only optimal in terms of sensitivity/specificity trade-off for Gaussian

---
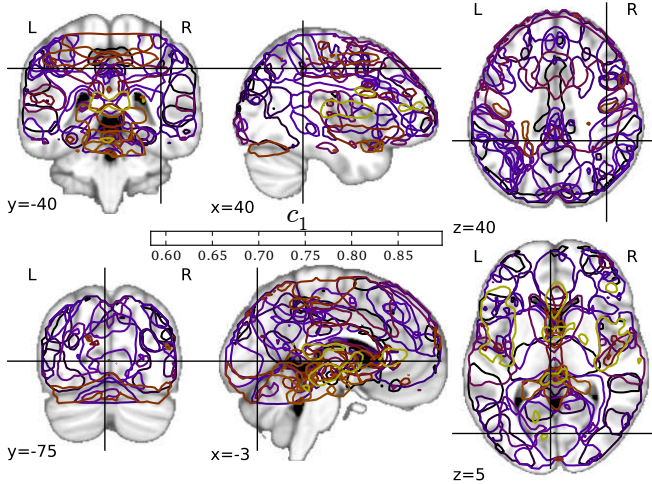
Fig. 1. Componentwise c_1 value, averaged across subjects.

populations. This means that potentially other statistics may provide more sensitive results in a nonparametric setting. Also, nonparametric testing refers here to the computation of the distribution under the null hypothesis using permutations [22].

Due to lack of space, we only report the t-score computations to test Assumptions (5):

$$\forall p = 1:2, \quad \forall k = 1:K, \quad T_{p,k} = \mu_{p,k}/\sqrt{S\sigma_{p,k}^2} \qquad (6)$$

$$\text{with} \quad \mu_{p,k} = \sum_{s=1}^{S} \widehat{c}_{p,k}^s/S, \quad \sigma_{p,k}^2 = \sum_{s=1}^{S}\left(\widehat{c}_{p,k}^s - \mu_{p,k}\right)^2/(S-1).$$

To account for the multiple comparison problem (K tests performed simultaneously) and apply correct specificity control (control of false positives), a proper calibration was elaborated using permutations [22]. However, given that only a few spatial components are involved in the statistical analysis, the Bonferroni correction alternative is not too conservative in the present study. The latter consists in dividing the componentwise t-score in Eq. (6) by K since K tests are performed for each cumulant $(c_{p,k})_{k=1}^K$.

The abovementioned tests allows one to perform nonparametric random-effect analysis. Since our analysis relies on [16], confidence intervals were also derived using bootstrap in addition to the log-cumulant estimates $(\widehat{c}_{p,k}^s)$. This enables the use of Mixed Effect group (MFX) statistics in which intra-subject variance also enters in the computation of group statistics, whatever its nature (t-score, WSR,...). The reader is referred to [22] for the computation of such statistics. In what follows, we only report MFX results.

4.3. Results and discussion

MFX statistical analysis on $c_{1,k}$ reveals that all components reject the null hypothesis $H_0^{(1,k)}$ (see Fig. 1). In other words, LRD (or self-similarity) exists in the resting-state data whatever the spatial component of interest. This means that $1/f$ behaviour in the power spectral density is a feature common to fMRI datasets of physiological artifacts, resting-state functional networks, white matter, ... This motivates the need for further and more precise investigation of the scaling properties: first, the use of a more stringent tests on $c_{1,k}$; second, taking into account of higher-order scaling (or multifractal)
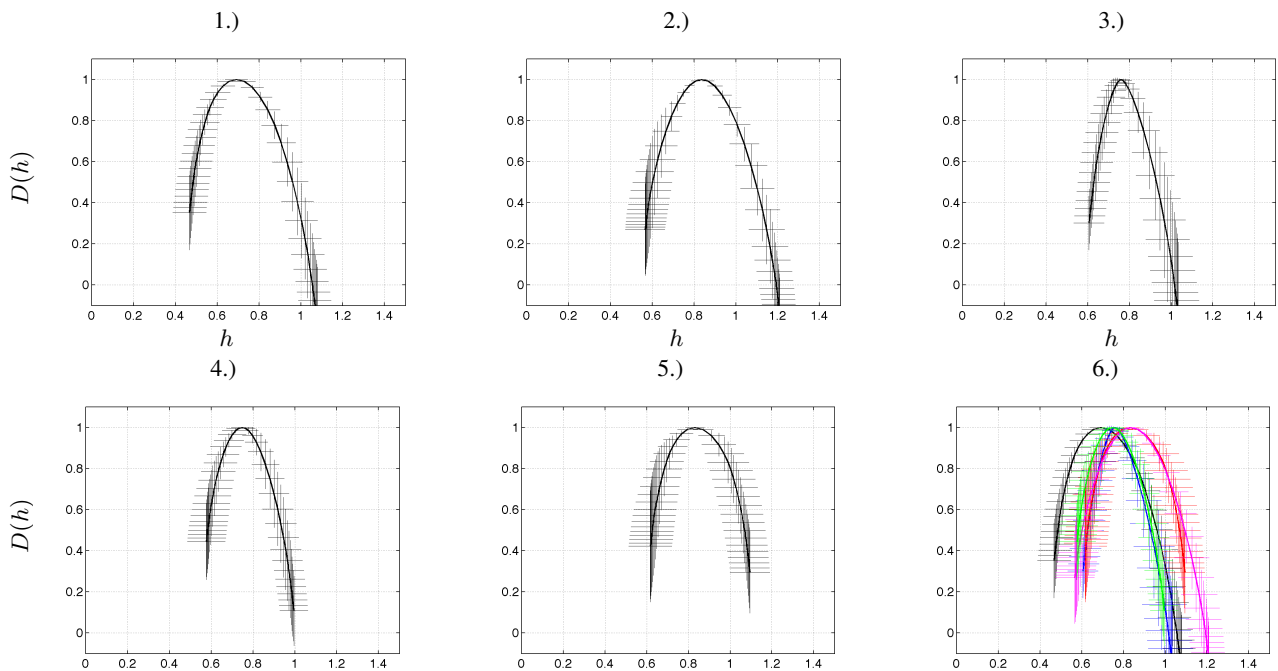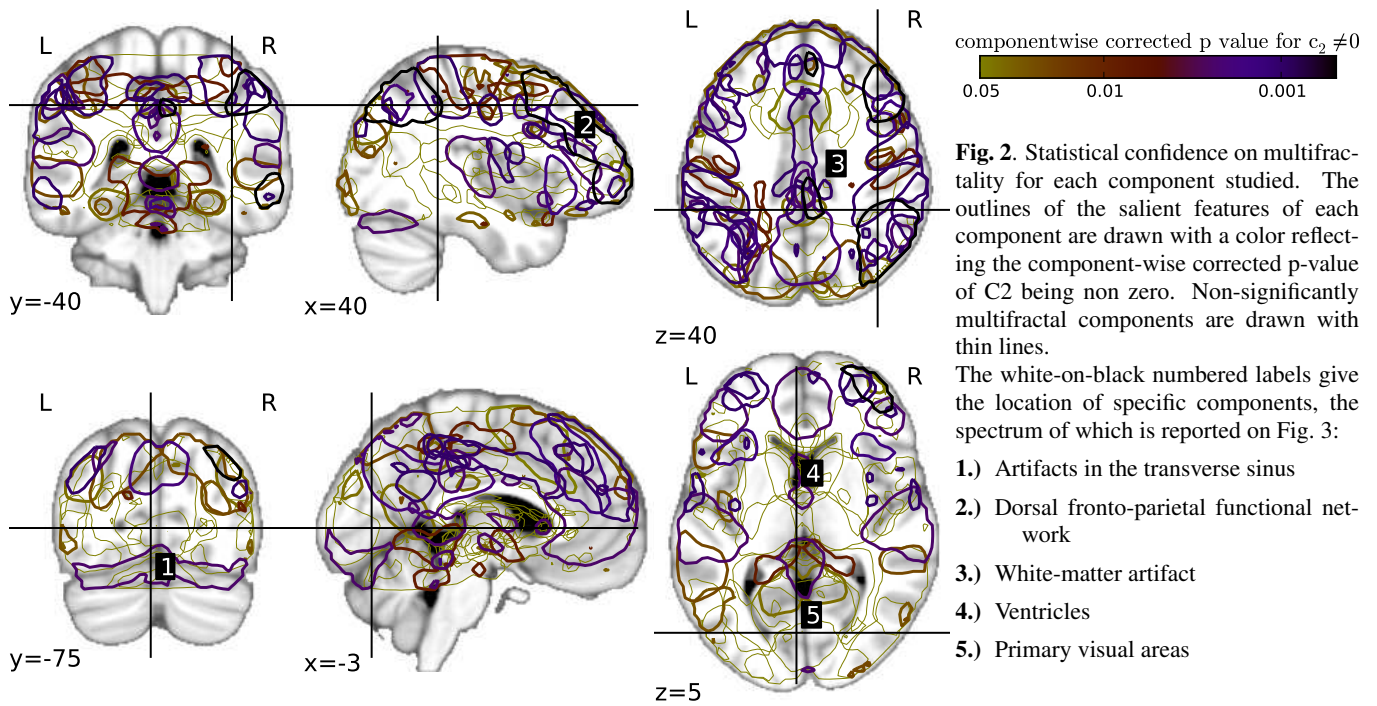
parameters. To cope with the first issue, we have investigated the null hypothesis $\widetilde{H}_0^{(1,k)} : c_{1,k} \leqslant 0.85$, and observed that it is rejected by only six components, found to correspond to the Dorso-parietal network and the primary visual areas, the Thalamus, the language network, the Parieto-cingulate network, and vascular noise in the circle of Willis. The first two regions are labeled respectively 2.) and 5.) in Fig. 2, while the last four ones are not referenced. For precise localization, see details in [19]. Regarding the second point, we have performed MFX analysis on $c_{2,k}$ to test $H_0^{(2,k)}$. Results are reported in Fig. 2. It appears that about 20 out of $K = 42$ spatial components significantly reject the null hypothesis $H_0^{(2,k)}$. For visualization purpose, the significant components, which have survived to a $p = .05$-thresholding, are color-coded, the less and most significant being displayed in yellow and purple/black, respectively.

In general, mutlifractality is found to be significant (very negative c_2) for components located in the gray matter and corresponding to functional networks, while self-similarity (or monofractality, $c_2 = 0$) is usually observed only in artifactual components or in the cerebro-spinal fluid. For instance, the component showing the most prominent multifractality ($\widehat{c}_2 = -0.075$) corresponds to the dorsal fronto-parietal functional RSN, referenced as 2.) in Fig. 2. Significant multifractality has also been found in the primary visual areas (V1 and V2 mainly), which are referenced as 5.) in Fig. 2. Nonetheless, there exist significant multifractal components that do not bring any relevant information on the cognitive side: for instance, artifact signals due to partial volume effects (see 1.) in Fig. 2) or times series associated with white matter (see 3.) in Fig. 2) or ventricles (cerebro-spinal fluid, see 4.) in Fig. 2) also exhibit non zero c_2 parameter. This suggests that our test is not strictly specific to resting-state functional connectivity networks.

Nonetheless, combining both tests, on $c_{1,k}$ and $c_{2,k}$ using $\widetilde{H}_0^{(1,k)}$ (with $c_{1,k} \leq 0.85$) and $H_0^{(2,k)}$, seems relevant to detect functional networks, as only the functional RSN 2.) and 5.) pass them. To bring evidence for this, we examine the *group-averaged* multifractal spectra $D(h)$ in Fig. 3, plotted for each of the five components reported in Fig. 2. Note that MF spectra $D(h)$ are actually computed as parametric functions of the statistical order q: $D(q)$ vs. $h(q)$ [11, 16] and that group-averaging takes place for each q value. Also, the horizontal and vertical error bars indicate incertainty or between-subject variability on $h(q)$ and $D(q)$, respectively. As expected theoretically, the larger $|q|$, the larger the uncertainties on $D(q)$ and $h(q)$. As expected empirically from the previous results, the MF spectra for components 2.) and 5.) are shifted to the right part of the x-axis because of larger c_1. These curves also emphasize a large Full-Width at Half Maximum (FWHM), which corroborates the high level of multifractality (large $|c_2|$). Note that component 1.) also exhibits a large value of $|c_2|$ but at the expense of a lower c_1, hence of a weaker long memory. The narrow spectra of components 3.) and 4.) and the location of their maximum confirm that they would not survive to more conservative hypothesis testing on $c2$ and c_1, respectively.

Fig. 2. Statistical confidence on multifractality for each component studied. The outlines of the salient features of each component are drawn with a color reflecting the component-wise corrected p-value of C2 being non zero. Non-significantly multifractal components are drawn with thin lines.

The white-on-black numbered labels give the location of specific components, the spectrum of which is reported on Fig. 3:

1.) Artifacts in the transverse sinus

2.) Dorsal fronto-parietal functional network

3.) White-matter artifact

4.) Ventricles

5.) Primary visual areas

Fig. 3. Group-averaged multifractal spectra and between-subject variability (ie standard deviation) for the outlined spatial components in Fig. 2: 1.) Cerebellum; 2.) Dorsal fronto-parietal network; 3.) White matter artifact; 4.) Ventricles; 5.) Primary visual areas and 6.) all the previous MF spectra are superimposed for visualization purpose with the following color-coding: 1.) 2.) ; 3.); 4.); 5.)

6. CONCLUSIONS

In this contribution, we have proposed to combine a group-level spatial ICA approach [19] with a recent multifractal analysis method based on wavelet leaders [16] to derive a multivariate scaling analysis approach of resting-state fMRI networks. Because the study takes place on a cohort of 12 subjects, group-level inference on multifractal parameters allows us to segregate brain regions that only generated strong long range dependence from those that exhibit multifractality as well. Among the latter, well-known functional resting-state networks were found as well as artifactual regions. A more thorough analysis of multifractal properties brings into light that the combination a large c_1 (strong long memory) and of a very negative c_2 (strong multifractality) appear specific of brain functional RSN, a potentially very important finding. Since the underlying mechanism of the BOLD signal and related vascular effects might also influence the mono vs multifractal behaviour, future work will also be devoted to the use of sparser spatial decompositions in order to better disentangle vascular and neural effects and to the analysis of activation datasets to investigate the impact of the hemodynamic variability [23] on MF attributes.

7. REFERENCES

[1] E. Zarahn, G. K. Aguirre, and M. D'Esposito, "Empirical analysis of BOLD fMRI statistics. I. Spatially unsmoothed data collected under null-hypothesis conditions," *Neuroimage*, vol. 5, no. 3, pp. 179–197, Apr. 1997.

[2] M. J. Mckeown, S. Makeig, G. G. Brown, T.-P. Jung, S. S. Kindermann, A. J. Bell, and T. J. Sejnowski, "Analysis of fmri data by blind separation into independent spatial components," *Hum. Brain Mapp.*, vol. 6, no. 3, pp. 160–188, 1998.

[3] Biyu J. He, John M. Zempel, Abraham Z. Snyder, and Marcus E. Raichle, "The temporal structures and functional significance of scale-free brain activity," *Neuron*, vol. 66, pp. 353–369, May 2010.

[4] P. L. Purdon and R. M. Weisskoff, "Effect of temporal autocorrelation due to physiological noise and stimulus paradigm on voxel-level false-positive rates in fMRI.," *Hum. Brain Mapp.*, vol. 6, no. 4, pp. 239–249, 1998.

[5] M. A. Burock, R. L. Buckner, M. G. Woldorff, B. R. Rosen, and A. M. Dale, "Randomized event-related experimental designs allow for extremely rapid presentation rates using functional MRI.," *Neuroreport*, vol. 9, no. 16, pp. 3735–3739, Nov. 1998.

[6] S. Thurner, E. Windischberger, C. Moser, P. Walla, and M. Barth, "Scaling laws and persistence in human brain activity," *Physica A*, vol. 326, no. 3, pp. 511–521, 2003.

[7] V. Maxim, L. Sendur, J. Fadili, J. Suckling, R. Gould, R. Howard, and E. Bullmore, "Fractional Gaussian noise, functional MRI and Alzheimer's disease.," *Neuroimage*, vol. 25, no. 1, pp. 141–158, mar 2005.

[8] K Linkenkaer-Hansen, S Monto, H Rytsala, K Suominen, E Isometsa, and S Kahkonen, "Breakdown of long-range temporal correlations in theta oscillations in patients with major depressive disorder.," *J Neurosci*, vol. 25, no. 44, pp. 10131–10137, Nov 2005.

[9] J. Fadili and E. Bullmore, "Wavelet-generalized least squares: A new BLU estimator of linear regression models with 1/f errors," *Neuroimage*, vol. 15, no. 1, pp. 217–232, Jan. 2002.

[10] Luo Huaien and Sadasivan Puthusserypady, "fMRI data analysis with nonstationary noise models: a Bayesian approach," *IEEE Trans. Biomed. Eng.*, vol. 54, no. 9, pp. 1621–1630, Sep. 2007.

[11] P. Ciuciu, P. Abry, C. Rabrait, and H. Wendt, "Log wavelet leaders cumulant based multifractal analysis of EVI fMRI time series: evidence of scaling in ongoing and evoked brain activity," *IEEE Journal of Selected Topics in Signal Processing*, vol. 2, no. 6, pp. 929–943, Dec. 2008.

[12] Yu Shimizu, Markus Barth, Christian Windischberger, Ewald Moser, and Stefan Thurner, "Wavelet-based multifractal analysis of fMRI time series.," *Neuroimage*, vol. 22, no. 3, pp. 1195–1202, Jul 2004.

[13] J.M. Lee, J. Hu, J.B. Gao, K.D. White, B. Crosson, C.E. Wierenga, K. McGregor, and K.K. Peck, "identification of brain activity by fractal scaling analysis of functional MRI data," in *30th Proc. IEEE ICASSP*, Philadelphia,, May 2005, vol. II, pp. 137–140.

[14] M.-E. Torres and P. Abry, "Comparison of different methods for computing scaling parameter in the presence of trends," in *14th BioIngineering argentin congress*, Argentine Cordoba, Ed., 2003.

[15] P. Ciuciu, P. Abry, C. Rabrait, H. Wendt, and Advanced Robotics, "Leader-based multifractal analysis for EVI fMRI time series: ongoing vs. task-related brain activity," in *4th Proc. IEEE ISBI*, Arlington, VA, Apr. 2007, pp. 404–407.

[16] H. Wendt, P. Abry, and S. Jaffard, "Bootstrap for empirical multifractal analysis," *IEEE Signal Proc. Mag.*, vol. 24, no. 4, pp. 38–48, 2007.

[17] C.F. Beckmann and S.M. Smith, "Probabilistic independent component analysis for functional magnetic resonance imaging," *IEEE Trans. Med. Imag.*, vol. 23, no. 2, pp. 137–152, 2004.

[18] G. Varoquaux, M. Keller, J.-B. Poline, P. Ciuciu, and B. Thirion, ," in *7th Proc. IEEE ISBI*, Rotterdam, The Netherlands, Apr. 2010, pp. 1177–1180.

[19] G. Varoquaux, S. Sadaghiani, Ph. Pinel, A. Kleinschmidt, J.-B. Poline, and B. Thirion, "A group model for stable multi-subject ICA on fMRI datasets," *Neuroimage*, vol. 51, no. 1, pp. 288–299, 2010.

[20] I. Daubechies, E. Roussos, S. Takerkart, M. Benharrosh, C. Golden, K. DArdenne, W. Richter, J. D. Cohen, , and J. Haxby, "Independent component analysis for brain fMRI does not select for independence," *PNAS*, vol. 106, no. 26, pp. 10415–10422, 2009.

[21] R. H. Riedi, "Multifractal processes," *in: "Theory and applications of long range dependence ", eds. Doukhan, Oppenheim and Taqqu*, pp. 625–716, 2003.

[22] S. Mériaux, A. Roche, G. Dehaene-Lambertz, B. Thirion, and J.-B. Poline, "Combined permutation test and mixed-effect model for group average analysis in fMRI.," *Hum. Brain Mapp.*, vol. 27, no. 5, pp. 402–410, May 2006.

[23] T. Vincent, L. Risser, and P. Ciuciu, "Spatially adaptive mixture modeling for analysis of within-subject fMRI time series," *IEEE Trans. Med. Imag.*, vol. 29, no. 4, pp. 1059–1074, Apr. 2010.